Demonstration of conditional gate operation using superconducting charge qubits

T. Yamamoto[1,2], Yu. A. Pashkin[2]*, O. Astafiev[2], Y. Nakamura[1,2] & J. S. Tsai[1,2]

[1]*NEC Fundamental Research Laboratories, Tsukuba, Ibaraki 305-8501, Japan*
[2]*The Institute of Physical and Chemical Research (RIKEN), Wako, Saitama 351-0198, Japan*

* Permanent address: Lebedev Physical Institute, Moscow 117924, Russia

Following the demonstration of coherent control of the quantum state of a superconducting charge qubit[1], a variety of qubits based on Josephson junctions have been implemented[2–5]. Although such solid-state devices are not currently as advanced as microscopic qubits based on nuclear magnetic resonance[6] and ion trap[7] technologies, the potential scalability of the former systems—together with progress in their coherence times and read-out schemes—makes them strong candidates for the building block of a quantum computer[8]. Recently, coherent oscillations[9] and microwave spectroscopy[10] of capacitively coupled superconducting qubits have been reported; the next challenging step towards quantum computation is the realization of logic gates[11,12]. Here we demonstrate conditional gate operation using a pair of coupled superconducting charge qubits. Using a pulse technique, we prepare different input states and show that their amplitude can be transformed by controlled-NOT (C-NOT) gate operation, although the phase evolution during the gate operation remains to be clarified.

A Cooper-pair box provides an artificial two-level system, where two charge states, say $|0\rangle$ and $|1\rangle$, differing by $2e$ of one Cooper pair (e is the electronic charge) are coherently superposed by Josephson coupling[13]. When two Cooper-pair boxes are connected by a capacitor, the quantum states of the boxes interfere with each other. This results in quantum beating, as has been demonstrated recently[9]. Using this coherent four-level system formed by the charge states $|00\rangle$, $|01\rangle$, $|10\rangle$ and $|11\rangle$, we show how to implement a logic gate and demonstrate that it works as a quantum gate.

A scanning electron micrograph of the sample is shown in Fig. 1a. Two qubits are electrostatically coupled by an on-chip capacitor[9]. The right qubit has SQUID (superconducting quantum interference device) geometry, and we use this qubit as the control qubit and the left one as the target qubit. Unlike the previous coupled-qubit sample[9], there are two independent pulse gates so that we can address each qubit individually. This is essential to the logic operation, as explained below.

In the two-qubit charge basis $|00\rangle$, $|10\rangle$, $|01\rangle$ and $|11\rangle$, the hamiltonian of the system is given as

$$H=\sum_{n_1,n_2=0,1}E_{n_1n_2}|n_1,n_2\rangle\langle n_1,n_2|-\frac{E_{J1}}{2}\sum_{n_2=0,1}(|0\rangle\langle 1|+|1\rangle\langle 0|)\otimes|n_2\rangle\langle n_2|-\frac{E_{J2}}{2}\sum_{n_1=0,1}|n_1\rangle\langle n_1|\otimes(|0\rangle\langle 1|+|1\rangle\langle 0|), \quad (1)$$

where E_{J1} (E_{J2}) is the Josephson coupling energy of the first (second) box to the reservoir and $E_{n_1n_2}=E_{c1}(n_{g1}-n_1)^2+$

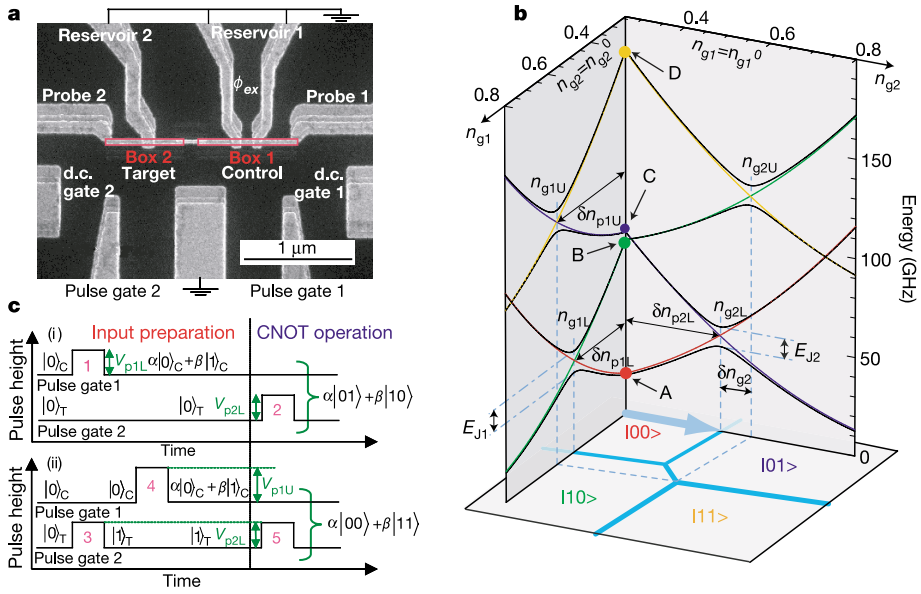

Figure 1 Pulse operation of the coupled-qubit device. **a**, Scanning electron micrograph of the sample. The qubits were fabricated by electron-beam lithography and three-angle evaporation of Al on a SiN_x insulating layer above a gold ground plane on the oxidized Si substrate. The two strips enclosed by red lines are the Cooper-pair boxes, which are coupled by an on-chip capacitor[9]. ϕ_{ex} represents magnetic flux penetrating the SQUID loop. An electrode between the two pulse gates is connected to the ground to reduce the cross capacitance. Although there is a finite cross capacitance between one gate and the other box (about 15% of the main coupling), it does not play any essential role in the present experiment and so we can neglect it in this Letter. The sample was cooled to 40 mK in a dilution refrigerator. The characteristic energies of this sample estimated from the d.c. current–voltage measurements are $E_{c1}=580\,\mu$eV, $E_{c2}=671\,\mu$eV and $E_m=95\,\mu$eV. From the pulse measurements, E_{J1} is found to be 45 μeV at a maximum and E_{J2} to be 41 μeV. The superconducting energy gap is 209 μeV. Probe junction tunnel resistance is equal to 48 MΩ (left) and 33 MΩ (right). **b**, Energy band diagram along two lines of $n_{g1}=n_{g1}^0$ and $n_{g2}=n_{g2}^0$, where n_{g1}^0 and n_{g2}^0 are constants. Here $(n_{g1}^0, n_{g2}^0)=(0.24,\ 0.26)$, corresponding to the actual experimental condition. In the energy band diagram, black lines show the eigenenergies. The four coloured lines are the charging energies of the states shown in the cells of the charging diagram of the base plane with the corresponding colour. **c**, Pulse sequences used in the experiment. In both sequences (i) and (ii), the upper and lower patterns show the pulse patterns applied to pulse gates 1 and 2, respectively. The expected quantum states after each pulse are also shown. The symbols $|0\rangle$ or $|1\rangle$ with subscripts C and T mean the state of the control and target qubits, respectively.

$E_{c2}(n_{g2}-n_2)^2+E_m(n_{g1}-n_1)(n_{g2}-n_2)$ is the total electrostatic energy of the system (n_1, $n_2=0$, 1 is the number of excess Cooper pairs in the first and second boxes, and $n_{g1,2}$ are the gate-induced charges on the corresponding qubit divided by $2e$). $E_{c1(2)}=4e^2C_{\Sigma2(1)}/2(C_{\Sigma1}C_{\Sigma2}-C_m^2)$ are the effective Cooper-pair charging energies ($C_{\Sigma1(2)}$ are the sum of all capacitances connected to the corresponding island including the coupling capacitance C_m between two boxes). Finally, $E_m=4e^2C_m/(C_{\Sigma1}C_{\Sigma2}-C_m^2)$ is the coupling energy. In our notation of $|n_1, n_2\rangle$ for the charge basis, n_1 and n_2 represent the states of the control and target qubits, respectively.

Figure 1b represents the idea for the gate operation. Using equation (1), we calculate the eigenenergies of the two-qubit system and plot them in the planes $n_{g1}=n_{g1}^0$ and $n_{g2}=n_{g2}^0$, where n_{g1}^0 and n_{g2}^0 are constants. In these planes, if (n_{g1}^0, n_{g2}^0) is sufficiently far away from the co-resonant point[9] (0.5, 0.5), four energy bands can be regarded as two pairs of nearly independent single-qubit energy bands. In the plane of $n_{g1}=n_{g1}^0$, for example, our system is divided into a pair of independent two-level systems $|00\rangle$, $|01\rangle$ and $|10\rangle$, $|11\rangle$. Importantly, the charging energies of each of the two-level systems degenerate at different n_{g2}, namely, at n_{g2L} for the states $|00\rangle$ and $|01\rangle$ and at n_{g2U} for the states $|10\rangle$ and $|11\rangle$, as shown in Fig. 1b. This difference (δn_{g2}) originates from the electrostatic coupling between the qubits, and is given as $E_m/2E_{c2}$. Similarly, we define n_{g1L} and n_{g1U} as shown in the plane of $n_{g2}=n_{g2}^0$.

Now we consider the pulse operation. Applying pulses to pulse gate 1 (2) shifts the system non-adiabatically in the plane of $n_{g2}=n_{g2}^0(n_{g1}=n_{g1}^0)$. For convenience, we define the distances from (n_{g1}^0, n_{g2}^0) to the degeneracy points as follows: $\delta n_{p1L}=n_{g1L}-n_{g1}^0$, $\delta n_{p1U}=n_{g1U}-n_{g1}^0$ and $\delta n_{p2L}=n_{g2L}-n_{g2}^0$. Suppose we start from the $|00\rangle$ state (point A) and apply an ideal rectangular pulse with an amplitude $V_{p2L}=2e\,\delta n_{p2L}/C_{p2}$ to pulse gate 2, where C_{p2} is the capacitance between pulse gate 2 and box 2. This pulse is represented by the arrow in the ground-state charging diagram[14] of the base plane. In this case, the system is brought to the degeneracy point n_{g2L} and evolves during a pulse duration Δt with a frequency $\Omega=E_{J2}/\hbar$ between the $|00\rangle$ and the $|01\rangle$ states: $\cos(\Omega\Delta t/2)|00\rangle+\sin(\Omega\Delta t/2)\,|01\rangle$. By adjusting Δt so that $\Omega\Delta t=\pi$ (π-pulse), we can stop the evolution when the system is in the $|01\rangle$ state. The system is finally in the state at point C after the termination of the pulse.

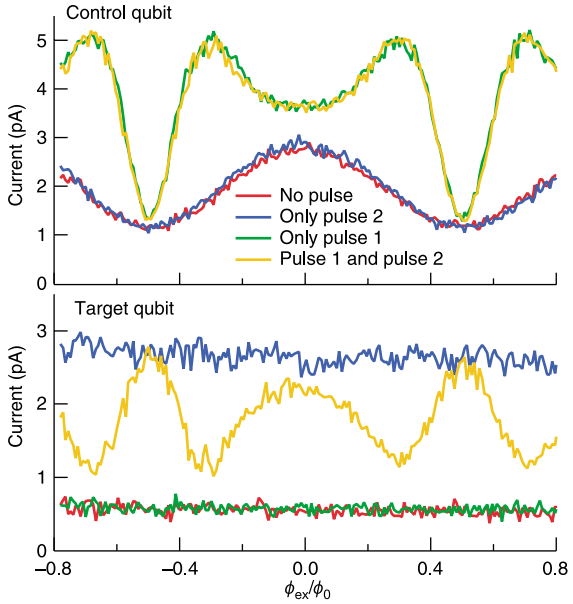

Figure 2 Magnetic-flux dependence of the current of the control (top) and target (bottom) qubits under the application of pulses shown in Fig. 1c (i). The lengths of the pulses are $\Delta t_1=85$ ps, $\Delta t_2=255$ ps and $\Delta t_{12}=85$ ps, where we define the pulse length of pulse m in Fig. 1c as Δt_m and the interval between pulses l and m as Δt_{lm}.

On the other hand, if we start from the $|10\rangle$ state (point B) and apply the same pulse, the system does not reach the degeneracy point for states $|10\rangle$ and $|11\rangle$ (n_{g2U}). In this case, the amplitude of the oscillation between the $|10\rangle$ and the $|11\rangle$ states is suppressed by $E_{J2}^2/(E_m^2+E_{J2}^2)$. If E_m is sufficiently large, the state $|10\rangle$ remains almost unchanged (except for the phase factor), coming back to point B after the termination of the pulse. Similarly, we can realize the transition from the $|01\rangle$ state to the $|00\rangle$ state by the same pulse, and suppress the transition out of the $|11\rangle$ state. Therefore, conditional gate operation can be carried out based on this operation pulse: the target bit is flipped only when the control bit is $|0\rangle$.

To experimentally demonstrate the above gate operation, we prepare different input states from the ground state $|00\rangle$ by applying pulses and measure the output of the gate operation. Figure 1c shows two pulse sequences that are used in the present experiment. For convenience, each of the pulses in the sequences is labelled by an index m ($m=1, \ldots, 4, 5$), which we will refer to as 'pulse m'. In sequence (i) of Fig. 1c, a superposition of the states $|00\rangle$ and $|10\rangle$ is created by applying pulse 1 with the amplitude $V_{p1L}=2e\,\delta n_{p1L}/C_{p1}$, where C_{p1} is the capacitance between pulse gate 1 and box 1. In sequence (ii) of Fig. 1c, a superposition of the states $|01\rangle$ and $|11\rangle$ is created by two sequential pulses. First, pulse 3, the same pulse as that for the gate operation, brings the system to the $|01\rangle$ state at point C. Then, pulse 4 with amplitude $V_{p1U}=2e\,\delta n_{p1U}/C_{p1}$ is applied.

In both sequences, an operation pulse (pulse 2 or 5) creating an

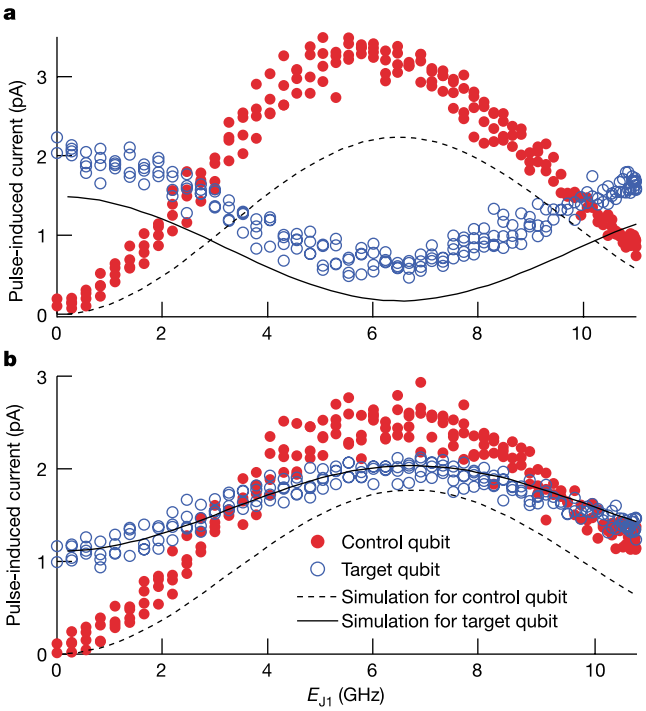

Figure 3 Pulse-induced current as a function of the Josephson energy of the control qubit. Pulse sequences used are **a**, that shown in Fig. 1c (i), and **b**, that shown in Fig. 1c (ii). The lengths of the pulses in Fig. 1c (ii) are $\Delta t_3=264$ ps, $\Delta t_4=88$ ps, $\Delta t_5=264$ ps, $\Delta t_{34}=88$ ps and $\Delta t_{45}=88$ ps. The black curves represent the simulation obtained by calculating the time evolution of the density matrix. In the calculation, we assumed a trapezoidal pulse shape with both rise and fall times equal to 40 ps, which is close to the real pulse shape. To take into account the effect of dephasing, all the off-diagonal terms of the density matrix are set to zero before applying the operation pulse. This is a reasonable approximation because the dephasing time at an off-degeneracy point is reported to be a few hundred picoseconds[16], which is comparable to the time needed for the input preparation for the present experiment. We did not take into account the energy relaxation, which is known to be much slower.

entangled state ($\alpha|01\rangle + \beta|10\rangle$ or $\alpha|00\rangle + \beta|11\rangle$) is applied after the preparation pulses. To change the coefficients α and β, we change the Josephson energy of the control qubit E_{J1} by a magnetic field, while keeping the pulse lengths constant. Because the control qubit has SQUID geometry, E_{J1} is periodically modulated as $E_{J1} = E_{J1max}|\cos(\pi\ \phi_{ex}/\phi_0)|$, where E_{J1max} is the maximum value of E_{J1} and ϕ_0 is the flux quantum. By repeatedly applying the sequential pulses (with a repetition time $T_r = 128$ ns), we measure the pulse-induced currents through probes 1 and 2, which are biased at $\sim$650 μV to enable a Josephson-quasiparticle (JQP) cycle[15]. These currents are proportional to the probability of the respective qubit having one extra Cooper pair[1,9].

Figure 2 shows the output currents of the control qubit (I_C) and the target qubit (I_T) as a function of ϕ_{ex}/ϕ_0 under the application of pulses shown in Fig. 1c (i). When no pulse is applied, both qubits show a finite current owing to the finite width of the JQP peak (red curves in Fig. 2). Because this current depends on the Josephson energy, I_C is periodically modulated by ϕ_{ex}. First, we determine the length of the operation pulse (pulse 2) by adjusting it to the peak in the single-qubit oscillation of I_T. When we apply pulse 2 of this length (blue curves in Fig. 2), I_T is enhanced and does not depend on ϕ_{ex}, as was expected. Also, this pulse has no effect on I_C. Next, we apply the preparation pulse (pulse 1) only. This pulse, in turn, induces current in I_C while not affecting I_T (green curves in Fig. 2).

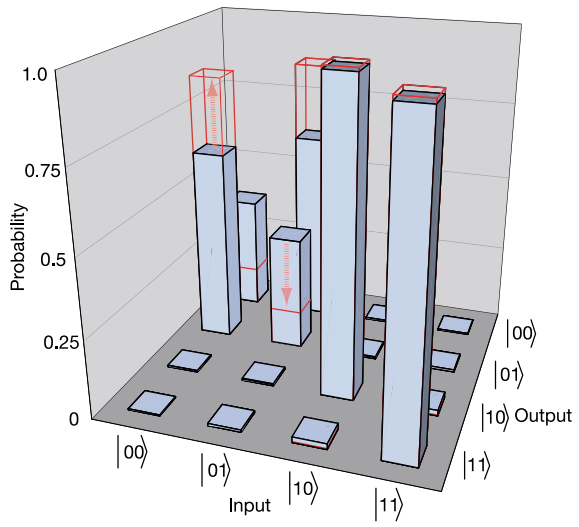

Figure 4 Truth table of the present C-NOT operation estimated by the numerical calculation (solid blue bars). Detailed values of the probabilities are

$$\begin{pmatrix} 0.37 & 0.62 & 0.004 & 0.003 \\ 0.62 & 0.37 & 0.004 & 0.007 \\ 0.004 & 0.004 & 0.97 & 0.018 \\ 0.003 & 0.007 & 0.018 & 0.97 \end{pmatrix}.$$

Ideally, they should be

$$\begin{pmatrix} 0 & 1 & 0 & 0 \\ 1 & 0 & 0 & 0 \\ 0 & 0 & 1 & 0 \\ 0 & 0 & 0 & 1 \end{pmatrix}.$$

We can partly see the correspondence of this figure to the experimental data in Fig. 3. Because the prepared input state in sequence (i) of Fig. 1c is almost pure $|00\rangle$ state when E_{J1} equals zero, the I_T at $E_{J1} = 0$ in Fig. 3a normalized by the possible maximum current $2e/T_r$ (2.5 pA) should be close to 0.62 (the second element of the first column of the above truth table). The experimental data gives a slightly larger value of $\sim$0.8. This is attributed to the leak current discussed in the text. The red lines and arrows indicate the expected improvement after decreasing the rise/fall time of the pulses from 40 to 30 ps.

Furthermore, the magnitude of the induced current depends on ϕ_{ex}, indicating that input states with different coefficients α and β are prepared. Finally, we apply both pulse 1 and pulse 2 with an interval of 85 ps (orange curves in Fig. 2). In this case, I_C shows the same dependence as that when only pulse 1 is applied. However, I_T also shows clear dependence on ϕ_{ex} and is anti-correlated with I_C as the target qubit feels the state of the control qubit. In Fig. 3a, we re-plot this data as a function of E_{J1}. We present only pulse-induced currents by subtracting the d.c. background currents from each curve. Both I_T and I_C show cosine-like dependence but their phases are opposite. That is, I_T is maximal when I_C is minimal, and vice versa. This is consistent with the expectation that the state $\alpha|01\rangle + \beta|10\rangle$ is created by the pulse sequence used.

Next we measure the ϕ_{ex} dependence of I_C and I_T for pulse sequence (ii) of Fig. 1c (not shown) and plot it as E_{J1} dependence in Fig. 3b. In this case, as in Fig. 3a, I_T and I_C show cosine-like dependence. However, most importantly, their correlation is now opposite to that in Fig. 3a. This is consistent with the expectation that the state $\alpha|00\rangle + \beta|11\rangle$ is created.

The above data show that we have succeeded with the conditional gate operation. However, to understand our results more quantitatively, we compare the data with simulation data obtained by numerically calculating the time evolution of the density matrix. The results of the simulation are shown as black curves in Fig. 3. We stress that no fitting parameters are used in the calculation.

First, we consider the target qubit. Apart from the offset in Fig. 3a, the simulated curves agree well with the experiment, suggesting that the oscillation amplitude of the measured I_T is reasonable. Second, in contrast, we have some discrepancy in I_C. We attribute this discrepancy to the unknown current channel in our present read-out scheme. As long as the JQP process is considered, the pulse-induced current should not be able to exceed $2e/T_r = 2.5$ pA, but in reality it does. This means that the pulse-induced current has an extra component that does not originate from the JQP process. We do not yet know the origin of this current. It may be other processes involving higher-order Cooper-pair tunnelling. The magnitude of this current probably depends on the Josephson energy (but does not depend strongly on the pulse length), and produces the E_{J1}-dependent deviation between the simulated and measured curves. In the target qubit, the similar current channel simply gives a constant offset in Fig. 3 as E_{J2} is fixed and does not affect the overall E_{J1}-dependence. Although quantitative analysis for I_C is difficult at present, the simulation suggests that the oscillation amplitude of the measured I_T is reasonable, whereas that of I_C is enhanced by this extrinsic factor originating from the imperfection of our read-out scheme.

Last, we estimate the accuracy of our gate operation and propose possible ways for improvement. Our present read-out scheme, which does not allow us to measure the probability of the four states individually[9], makes it difficult to obtain the complete truth table of our gate operation solely from the experimental data. Instead, here we do it on the basis of the simulation that turned out a reasonable description of our two-qubit system, as shown in Fig. 3. We calculate the time evolution of four perfect input states, $|00\rangle$, $|01\rangle$, $|10\rangle$ and $|11\rangle$, under the application of the operation pulse, namely pulse 2 or 5 in Fig. 1c, and plot the output probabilities as solid blue bars in Fig. 4. For the input states of $|10\rangle$ and $|11\rangle$, our gate operation is almost ideal. Note that the accuracy is better than that expected for the case of the ideal pulse shape, that is, $1 - E_{J2}^2/(E_m^2 + E_{J2}^2) \approx 0.84$. This is due to the finite rise/fall time (40 ps) of the operation pulse, which suppresses the unwanted oscillation. On the other hand, for the input states of $|00\rangle$ and $|01\rangle$, the output states have an unwanted component of $|00\rangle$ or $|01\rangle$ with a rather high probability. This is also due to the finite rise/fall time, which in this case suppresses the desired oscillation. To improve this, increasing E_m as well as making the pulse shape ideal would be the best solution. However, even with the present value of

E_m, the simulation suggests that this matrix becomes much closer to the ideal one (keeping almost ideal outputs for $|10\rangle$ and $|11\rangle$ input states) if we slightly decrease the rise/fall time, say by 25% (red lines in Fig. 4), or decrease E_{J2} by a similar amount.

We controlled our two-qubit solid-state circuit by applying a sequence of pulses, and demonstrated the conditional gate operation. Although in the present experiment we paid attention only to the amplitude of the quantum state, phase evolution during the gate operation should also be examined for the realization of the quantum C-NOT gate (probably with additional phase factors), which is a constituent of the universal gate. □

Received 25 June; accepted 19 August 2003; doi:10.1038/nature02015.

1. Nakamura, Y., Pashkin, Yu. A. & Tsai, J. S. Coherent control of macroscopic quantum states in a single-Cooper-pair box. *Nature* **398,** 786–788 (1999).
2. Vion, D. *et al.* Manipulating the quantum state of an electrical circuit. *Science* **296,** 886–889 (2002).
3. Yu, Y., Han, S., Chu, X., Chu, S.-I. & Wang, Z. Coherent temporal oscillations of macroscopic quantum states in a Josephson junction. *Science* **296,** 889–892 (2002).
4. Martinis, J. M., Nam, S., Aumentado, J. & Urbina, C. Rabi oscillations in a large Josephson-junction qubit. *Phys. Rev. Lett.* **89,** 117901 (2002).
5. Chiorescu, I., Nakamura, Y., Harmans, C. J. P. M. & Mooij, J. E. Coherent quantum dynamics of a superconducting flux qubit. *Science* **299,** 1869–1871 (2003).
6. Vandersypen, L. M. K. *et al.* Experimental realization of Shor's quantum factoring algorithm using nuclear magnetic resonance. *Nature* **414,** 883–887 (2001).
7. Gulde, S. *et al.* Implementation of the Deutsch-Jozsa algorithm on an ion-trap quantum computer. *Nature* **421,** 48–50 (2003).
8. Nielsen, M. A. & Chuang, I. L. *Quantum Computation and Quantum Information* (Cambridge Univ. Press, Cambridge, UK, 2000).
9. Pashkin, Yu. A. *et al.* Quantum oscillations in two coupled charge qubits. *Nature* **421,** 823–826 (2003).
10. Berkley, A. J. *et al.* Entangled macroscopic quantum states in two superconducting qubits. *Science* **300,** 1548–1550 (2003).
11. Shnirman, A., Schön, G. & Hermon, Z. Quantum manipulations of small Josephson junctions. *Phys. Rev. Lett.* **79,** 2371–2374 (1997).
12. Averin, D. V. Adiabatic quantum computation with Cooper pairs. *Solid State Commun.* **105,** 659–664 (1998).
13. Bouchiat, V., Vion, D., Joyez, P., Esteve, D. & Devoret, M. H. Quantum coherence with a single Cooper pair. *Phys. Scripta* **T76,** 165–170 (1998).
14. Pothier, H., Lafarge, P., Urbina, C., Esteve, D. & Devoret, M. H. Single-electron pump based on charging effects. *Europhys. Lett.* **17,** 249–254 (1992).
15. Fulton, T. A., Gammel, P. L., Bishop, D. J., Dunkleberger, L. N. & Dolan, G. J. Observation of combined Josephson and charging effects in small tunnel junction circuits. *Phys. Rev. Lett.* **63,** 1307–1310 (1989).
16. Nakamura, Y., Pashkin, Yu. A., Yamamoto, T. & Tsai, J. S. Charge echo in a Cooper-pair box. *Phys. Rev. Lett.* **88,** 047901 (2002).

Acknowledgements We thank B. L. Altshuler, D. V. Averin, S. Ishizaka, F. Nori, T. Tilma, C. Urbina and J. Q. You for discussions.

Competing interests statement The authors declare that they have no competing financial interests.

Correspondence and requests for materials should be addressed to T.Y. (yamamoto@frl.cl.nec.co.jp).

High-*Q* photonic nanocavity in a two-dimensional photonic crystal

Yoshihiro Akahane[1,2], Takashi Asano[1], Bong-Shik Song[1] & Susumu Noda[1]

[1]*Department of Electronic Science and Engineering, Kyoto University, Katsura, Nishikyo-ku, Kyoto 615-8510, Japan*
[2]*Advanced Materials R&D Laboratories, Sumitomo Electric Industries, Ltd, Itami, Hyogo 664-0016, Japan*

Photonic cavities that strongly confine light are finding applications in many areas of physics and engineering, including coherent electron–photon interactions[1], ultra-small filters[2,3], low-threshold lasers[4], photonic chips[5], nonlinear optics[6] and quantum information processing[7]. Critical for these applications is the realization of a cavity with both high quality factor, *Q*, and small modal volume, *V*. The ratio *Q*/*V* determines the strength of the various cavity interactions, and an ultra-small cavity enables large-scale integration and single-mode operation for a broad range of wavelengths. However, a high-*Q* cavity of optical wavelength size is difficult to fabricate, as radiation loss increases in inverse proportion to cavity size. With the exception of a few recent theoretical studies[8–10], definitive theories and experiments for creating high-*Q* nanocavities have not been extensively investigated. Here we use a silicon-based two-dimensional photonic-crystal slab to fabricate a nanocavity with $Q = 45{,}000$ and $V = 7.0 \times 10^{-14}$ cm^3; the value of *Q*/*V* is 10–100 times larger than in previous studies[4,11–14]. Underlying this development is the realization that light should be confined gently in order to be confined strongly. Integration with other photonic elements is straightforward, and a large free spectral range of 100 nm has been demonstrated.

The *Q* of a cavity is determined by the energy loss per cycle versus the energy stored. With no absorption by the cavity material, *Q* is determined by the reflection loss at the interface between the interior and exterior of the cavity. Total internal reflection (TIR) and/or Bragg reflection are generally used for light confinement. For a cavity with a size much larger than the wavelength of light, a very high *Q* has already been achieved[14,15]. In that case, the behaviour of light confined in a large cavity obeys ray optics theory, and each ray of light reflected at the interface can be designed to fulfil TIR or Bragg reflection conditions. For much smaller cavities, deviation from ray optics becomes serious, and *Q* is greatly reduced. Light confined in a very small cavity consists of numerous plane wave components with wavevectors ($\mathbf{k}$) of various magnitudes (k) and directions owing to the localization of light. As it is difficult to design all such plane wave components to obey TIR or Bragg reflection conditions, photonic nanocavities with very high *Q* factors have yet to be realized.

One of the best approaches to resolving the problem is the extension of the Bragg reflection effect in multiple directions. Structures having a two- or three-dimensional (2D or 3D) periodic change of refractive index on the scale of the light wavelength are required for such extension. These are known as photonic crystals, from an analogy to solid crystals[5,16]. For a 3D photonic crystal, Bragg reflection conditions can be fulfilled for all the propagation directions of light in a certain frequency range, known as the photonic bandgap. A small disorder or defect introduced into the 3D photonic crystal would become an ultimate photonic nanocavity, with ultra-large *Q*/*V*. However, 3D photonic crystals with sufficiently strong optical confinement have yet to be created[5].

A cavity surrounded by a 2D photonic crystal is considered a feasible solution. A 2D photonic-crystal slab, as shown in Fig. 1a, with a thickness of the order of the light wavelength is very promising, owing to strong optical confinement for both in-plane and vertical directions[2,3]. The photonic-bandgap effect is used for light confinement in the in-plane direction, and TIR, at the interface between the slab and the air clad, in the vertical direction. Apparently, fulfilment of the TIR condition in the vertical direction is crucial in designing high-*Q*/*V* cavities.

To investigate vertical confinement in 2D photonic-crystal slabs, we first consider a simplified model (Fig. 2a), where the cavity consists of a dielectric material with thickness *T* and length *L*. Both sides of the cavity are closed by perfect mirrors, confining light in the *x* direction. The structure is assumed to be uniform in the *y* direction for simplicity. Light is confined by TIR in the *z* direction by the air clad, as discussed above. Figure 2b shows an example of the electric field profile inside a cavity with a very short length, 2.5λ, where λ is the resonant wavelength of light in the cavity.

The strength of the vertical (*z*-direction) confinement by TIR can be investigated by decomposing the electric field inside a cavity into a set of plane wave components with various $\mathbf{k}$-vectors by spatial

